CHEMICAL & BIOMEDICAL IMAGING

pubs.acs.org/ChemBioImaging

Article

Mapping Nanoscale Forces and Potentials in Live Cells with Microsecond 3D Single-Particle Tracking

Shangguo Hou,*,§ Chen Zhang,§ Anastasia Niver, and Kevin D. Welsher*

Cite This: https://doi.org/10.1021/cbmi.5c00293

Read Online

ABSTRACT: 3D single-particle tracking has the potential to resolve the molecular-level forces that dictate particle motion in biological systems. However, the information gleaned from 3D single-particle tracking often cannot resolve underlying nanoscale potentials due to limited spatiotemporal resolution. To this end, we introduce an active-feedback 3D tracking microscope that utilizes silver nanoparticles (AgNPs) as probes to study intricate biophysical events in live cells at the nanometer and microsecond scales. Due to the extremely high, durable scattering photon flux of the plasmonic particles, a 1 MHz sampling frequency with nanometer precision in all three dimensions can be achieved over an unlimited observation duration. In this work, microsecond-sampling, active-feedback 3D single-particle tracking was applied to investigate the interaction between AgNPs and nanoscale filopodia on the live-cell surface. The nanometer precision and microsecond sampling revealed that TAT peptide-modified particles visit and dwell at local "hot spots" on the filopodium surface. The high sampling rate further enabled the calculation of local forces and potentials within these nanoscale hotspots on the cylindrical surfaces of live-cell filopodia. This study presents a promising tool for investigating intracellular biophysical events with unprecedented spatiotemporal resolution, along with a pipeline for studying nanoscale potentials within three-dimensional cellular structures.

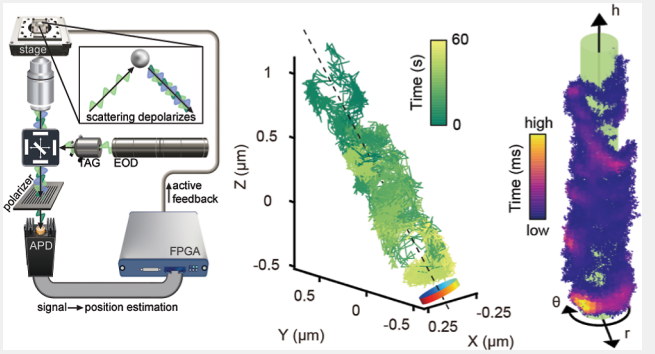

KEYWORDS: *3D single-particle tracking, microrheology, filopodia, plasmonic nanoparticles, scattering detection*

INTRODUCTION

Tracking particles in three dimensions can reveal the molecular forces and potentials that act on a moving particle in a complex environment.[1] In short, the trajectory of a single particle is a map of its interactions with the environment. For example, a particle may randomly diffuse among areas with different viscosity,[2,3] be pushed or pulled by molecular motors,[4] be physically trapped in a confined region due to steric obstruction,[5,6] or be tethered in a potential well by molecular interactions.[7] However, the information gleaned from particle trajectories is strongly determined by the spatiotemporal precision of each point in the path. Interactions smaller than the localization precision or more fleeting than the temporal resolution remain unresolved. Furthermore, trajectories must be long enough to allow the particle to map out an entire surface and measure its diffusive and other properties with sufficient resolution. Pulling molecular-scale information from single trajectories requires spatiotemporal precision commensurate with the forces and potentials at play.

Traditional 3D single-particle tracking methods have shown that particles will undergo random (Brownian) motion in solution, as well as a variety of confined diffusions with distinct geometries, such as diffusion along linear axes,[8] cell surfaces,[9] or isolated compartments.[10] Decoding the hidden information behind diffusion requires high spatiotemporal resolution. An example is the progressive stepwise motion of motor proteins, which exhibit a step size of 8 nm.[11] Resolving such features requires methods with localization precision on the order of several nanometers.[12] With advances in localization precision, it has been shown that previously considered nonmoving particles undergo restricted diffusion, and that the difference in their slow diffusive speed correlates with the fate of these vesicles.[13] Despite stunning progress in localization precision over the past two decades, advances in temporal resolution have lagged, largely due to the limited emission capacity of conventional fluorophores. This speed limit is magnified in 3D localization, leaving an underexplored field to be addressed with high spatiotemporal resolution methodologies. Of course, spatial and temporal resolution are intertwined. The ultimate

Received: December 30, 2025
Revised: April 1, 2026
Accepted: April 14, 2026

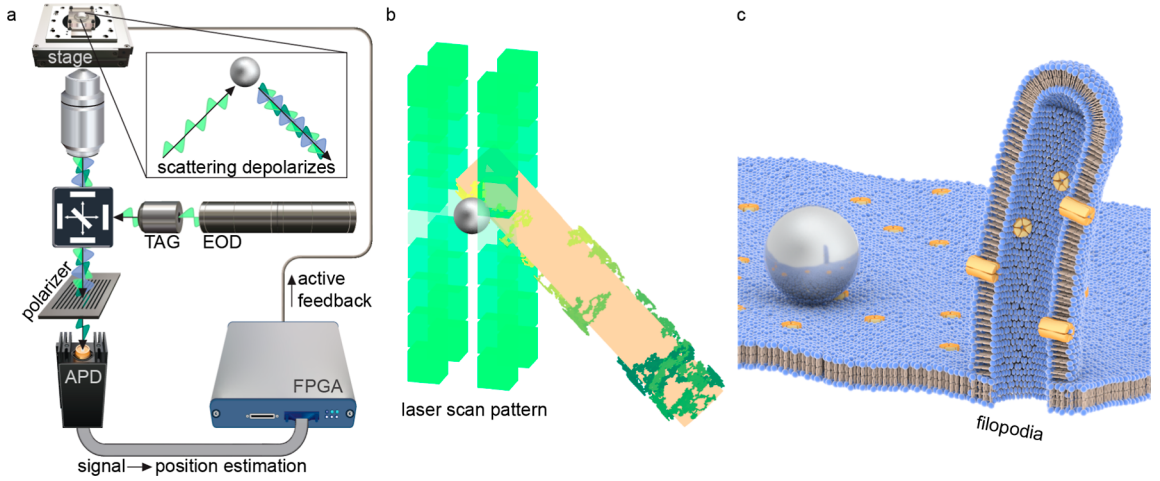

Figure 1. 3D-SMARTER. (**a**) Schematic of 3D-SMARTER setup. (**b**) Information-efficient sampling pattern implemented in 3D-SMARTER. Green boxes demonstrate areas in the vicinity of an AgNP (gray sphere) scanned. The AgNP is actively diffusing outside a cylindrical structure, leaving a time-coded trajectory recorded in real-time. (**c**) Schematic of the interaction between AgNP and live-cell filopodia probed by 3D-SMARTER.

spatial precision scales as $\frac{\sigma}{\sqrt{N}}$, where σ is the size of the point-spread function (PSF) and N is the number of photons collected.[14] The size of the PSF depends on the wavelength of light used and the numerical aperture of the collection objective. These two factors put a firm limit on the diffraction-limited spatial resolution. Even so, with the collection of many photons, the localization precision can be dramatically improved. However, fluorescence is limited in increasing the number of detected photons at short time scales due to saturation and finite fluorescence lifetime.[15] Therefore, scattering is an ideal choice for increasing both spatial and temporal resolution simultaneously. A scattering-based method with several-nanometer localization precision, submillisecond temporal resolution, and a large field of view in 3D is needed to extract maximal information from particle trajectories.

One candidate for such a method is real-time 3D single-particle tracking (RT-3D-SPT).[16−26] RT-3D-SPT utilizes active-feedback mechanisms to lock the target in the microscope's focus, enabling long-duration and high spatiotemporal resolution observation in three dimensions. RT-3D-SPT is emerging as a powerful tool for studying biological interactions due to its ability to unveil heterogeneity hidden within ensemble-averaged measurements and its compatibility with living systems.[27] Recently, 3D-SPT has been used in various scenarios to unveil new biological insights, including the visualization of changes in diffusion patterns in endocytic transport,[28] visualization of complex landing events of DNA-labeled NPs onto cells,[29] and the understanding of the search mechanism between CRISPR-Cas9 complex and its binding sites.[30] However, several limitations of current RT-3D-SPT methods stem from their reliance on fluorescent probes. First, conventional fluorescent particles emit only a finite number of photons before irreversible photobleaching, limiting the total duration of single-particle trajectories. Second, the emission rate of these particles is also limited and acts as a barrier to the temporal resolution of RT-3D-SPT, which is limited only by the photon collection rate. Highly scattering plasmonic nanoparticles (NPs) are a promising alternative due to their superior photostability and good biocompatibility. Plasmonic resonance on metal surfaces has been widely used in single-molecule sensing, Raman scattering detection, and super-resolution imaging.[31−37] In this work, it was observed that linearly polarized light can be depolarized upon scattering by plasmonic nanoparticles (e.g., silver nanoparticles, AgNPs). Consequently, a depolarized scattered-light detection method was employed to enhance the signal-to-background ratio for AgNP detection. By introducing a polarizer into the detection path, the reflected light from the coverslip can be substantially filtered out when the polarization angle of the polarizer is orthogonal to the polarization angle of the incident light. In contrast, the depolarized scattered light from the AgNP is retained. This approach effectively enhances the signal-to-background ratio for AgNP detection (Supplementary Figure S3). Similar to conventional fluorescence detection, in which wavelength is used to distinguish fluorescence from excitation light, polarization is a distinctive characteristic of the scattered light from AgNP in this method. Moreover, as the scattering light has the same wavelength as the incident light, background from autofluorescence can be removed with a narrow bandpass optical filter (Figure 1a). Most importantly, the scattered photons are not susceptible to photobleaching, quenching, or photoblinking. These features make scattering NPs ideal materials for real-time observation of cellular events with prolonged duration and high spatiotemporal precision.

Various studies have demonstrated the ability to obtain a high photon flux and high precision from gold and silver NPs in single-particle tracking studies.[4,38−40] Among those, dark-field and interferometric scattering (iSCAT) microscopies have shown great promise as single-particle tracking methods.[41−43] Dark field microscopy has shown great success in three-dimensional tracking and beyond,[44,45] but its temporal resolution is typically restricted by camera readout times. Meanwhile, the axial detection range of iSCAT microscopy is limited to several micrometers due to a complex axial PSF.[46] In contrast, RT-3D-SPT is ideally suited to take advantage of highly scattering metal nanoparticles. Whereas most microscopy methods rely on cameras, RT-3D-SPT uses single-photon-counting detectors that continuously track the target particle's location. In principle, the location of the particle can be updated with each arriving photon. For a scattering particle where MHz or greater photon detection rates are possible, the temporal resolution can be pushed into the submicrosecond

https://doi.org/10.1021/cbmi.5c00293
Chem. Biomed. Imaging XXXX, XXX, XXX−XXX

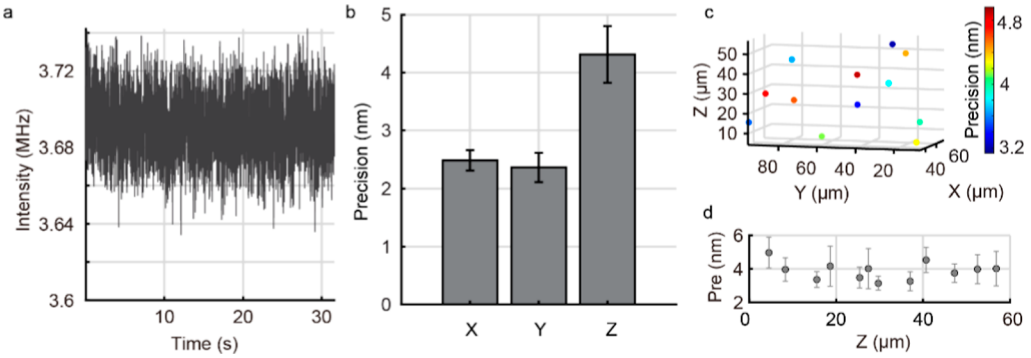

Figure 2. Precision and imaging depth of 3D-SMARTER. (**a**) Intensity trace from tracking an immobilized AgNP. Bin time: 1 ms. (**b**) Standard deviation of stage readout of X, Y, and Z axes while tracking of immobilized AgNPs. Standard deviation was calculated on 1 s segments, resulting in X, Y, and Z precision of 2.5 ± 0.2 nm, 2.4 ± 0.2 nm and 4.3 ± 0.5 nm, respectively (n = 31 1 s segments). Stage positions were sampled at 1 kHz. (**c**) Positions of 12 different AgNPs immobilized in Fluoromount medium at different depths in Z. (d) Tracking precision as a function of tracking depth. The coverslip surface is located at Z = 0 μm.

regime. RT-3D-SPT promises to be an ideal platform for scattering observation in biological studies, with temporal resolution no longer limited by camera exposure or readout times. While several studies have demonstrated the capability to track highly scattering NPs with RT-3D-SPT,[47−49] these methods have thus far only been demonstrated in vitro and have not been translated to a live-cell scenario.

In this study, we incorporated the detection of scattered and depolarized light from silver nanoparticles (AgNPs) into the previously reported 3D single-molecule active real-time tracking (3D-SMART) microscopy (Figure S1)[50] with an information-efficient sampling pattern[51] (Figures 1b, S2). In the XY-plane the laser scans 4 corners of a square with 20 μs dwell time. Along the Z-axis the laser follows a sine wave with ∼70 kHz frequency, leaving edges slightly more frequently scanned. This new method, incorporating high photon count rates and information-optimized scanning, is named 3D-SMARTER (Single Metal-nanoparticle Active Real-time Tracking with Enhanced Resolution). The detected depolarized scattering signal from AgNPs can reach 3 million photons per second, providing unprecedented spatial and temporal resolution in three dimensions while maintaining a large tracking depth and long observation time. In this work, we obtained 2.5 ± 0.2 nm localization precision in XY and 4.3 ± 0.5 nm precision in Z over a 50 μm axial range, with a temporal resolution down to 1 μs. The high spatial and temporal resolution of 3D-SMARTER enables observation of step motion of motor proteins in live cells and particle diffusion on complex, nanoscale 3D structures on the cell surface (Figure 1c). Not only did the high spatial resolution of 3D-SMARTER carve out a superresolved structure of cell surface filopodia, the high temporal resolution also uncovered local hot spots on the surface of these nanoscale cylindrical protrusions that were repeatedly visited by single particles. Recent studies have shown that rich information, such as sub-10 nm scale stepwise motion of microtube-associated proteins[52] or characterization of chromatin-interacting proteins,[53] can be extracted from observed confinement in single-particle trajectories. The rapid sampling of 3D-SMARTER enabled mapping of force vectors and potentials within these hot spots, untangling them from random Brownian motion and localization uncertainty. These analyses are only possible with spatial and temporal precision better than the feature in question. 3D-SMARTER is a powerful tool to study biological events with unprecedented spatiotemporal precision.

RESULTS

Tracking of AgNPs with High Precision Deep within Samples

3D-SMART has been previously applied to track fluorescent protein-tagged virus-like particles in live cells[54,55] and single fluorescent Atto 647N dye-labeled proteins and nucleic acids in solution.[50] As noted above, in each case, the photobleaching of fluorescent tags limits the signal rate and observation time. 3D-SMARTER was built upon the previously reported 3D-SMART platform. Briefly, an electro-optic deflector (EOD) and tunable acoustic gradient (TAG) lens are applied to rapidly shift the laser focus in a restricted volume in the vicinity of the particle (1 μm × 1 μm × 2 μm, XYZ). Real-time photon arrival information is then used to estimate the particle position within the scan area and used to guide a piezoelectric stage to actively track the target. Photons are collected on a single-photon counting avalanche photodiode, which has a saturating count rate of 12 MHz. Real-time localization is performed using a Kalman filter[56] on a field-programmable gate array (FPGA) as described in prior implementations of 3D-SMART.[24,50] Two major changes were applied to utilize the exceptional brightness and unique scattering mechanism of AgNPs. First, a polarizer was added to the detection path. The polarization angle of this polarizer was set perpendicular to the polarization angle of the excitation laser to maximize contrast of the scattering nanoparticle (Figure S3). Second, rather than the previously reported 5 × 5 grid Knight's Tour pattern, an information-efficient 4-pixel pattern (4-Corners pattern) that only samples areas with high Fisher information was used.[51] The information-optimized 4-Corners pattern enables the extraction of maximal information from the scattering signal. Critically, with the same 20 μs pixel dwell time used, the 4-Corners pattern leads to an 80 μs period of a single scan cycle, dramatically shorter than the 500 μs cycle of the previously used Knight's Tour pattern, enabling a greatly enhanced sampling rate.

To evaluate the robustness of the 3D-SMARTER mechanism, 100 nm PEG-AgNPs (2 pM, KJW1912, NanoComposix) were diluted into water and tracked in aqueous solution. 3D-SMARTER was able to track freely diffusing 100 nm AgNPs in aqueous solution, and the measured diffusion coefficient is

https://doi.org/10.1021/cbmi.5c00293
Chem. Biomed. Imaging XXXX, XXX, XXX−XXX

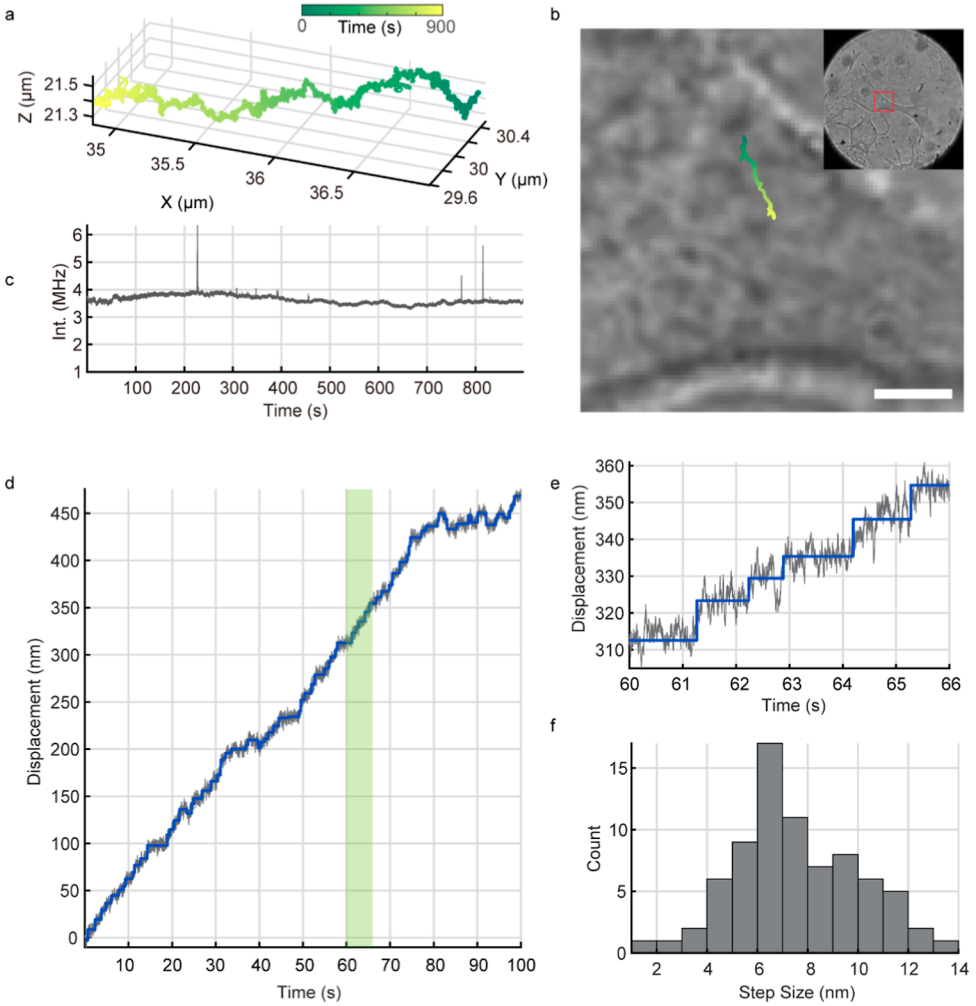

Figure 3. Characterization of motor protein motion in live cells by 3D-SMARTER. (a) 3D trajectory of a 100 nm AgNP in a live HeLa cell. (b) Bright-field image of the cell overlapped with the trajectory in (a) obtained after the trajectory was collected by 3D-SMARTER. Scale bar: 2 μm. Insert: larger view of the cell. (c) Depolarized scattering intensity trace of the trajectory in (a). (d) Displacement in lateral motion along an axis parallel to the observed linear motion from 610 to 710s of the trajectory in (a). (e) A closer look at (d) with steps labeled by a light green shadow. (f) Step size histogram. Mean step size = 7.6 ± 2.5 nm (n = 76).

around 4 $\mu m^2/s$ (Figures S4, S19), which is comparable to previously reported results obtained from fluorescent materials with 3D-SMART. We note here that the laser powers used (640 nW) have a negligible effect on the motion of AgNPs. Furthermore, the power density of the focused laser spot it 0.45 kW/cm^2, well within the range for viable cell imaging.[57] This focused spot is constantly scanned over a 0.5 × 0.5 × 1 μm^3 volume, and its centroid moves along with the particle, minimizing continuous exposure to any one part of the cell. To evaluate the localization precision of the method, citrate-stabilized AgNPs (2 pM, AGCB100−1M, NanoComposix) were diluted into PBS and particles bound to the coverslip were tracked with 3D-SMARTER. The intensity trace of an immobilized AgNP being actively tracked is shown in Figure 2a. The depolarized scattering signal is extremely stable with a count rate of ∼3.7 MHz. This ample photon flux enabled nanoscale precision in all three dimensions. The tracking precision obtained for immobilized AgNPs was 2.5 ± 0.2 nm, 2.4 ± 0.2 nm, and 4.3 ± 0.5 nm, for X, Y, and Z, respectively (Figure 2b). This high precision was maintained at significant depth within the sample. To demonstrate, 100 nm AgNPs were diluted to ∼1 pM into Fluoromount mounting medium (Sigma, F4680). The resulting suspension was sandwiched between two coverslips, heated to fix the sample, and mounted on the microscope to track immobilized AgNPs at various depths. As shown in Figure 2c, nanoscale localization of the AgNPs could be achieved over a range of more than 50 μm in Z, far beyond the several-micron imaging depth of other scattering-based detection methods.[46] Importantly, combined tracking precision (standard deviation of stage positions), which is defined as $P_{comb} = \frac{1}{3}\sqrt{P_x^2 + P_y^2 + P_z^2}$, did not vary with depth within the sample (Figure 2d). Apart from high spatial precision, AgNPs were observed to retain MHz emission rate for tens of minutes (Figure S18a), demonstrating superiority in terms of brightness and duration over conventional fluorescent (Figure S18b−c).

Characterization of Cargo Motion in Live Cells

To demonstrate the benefits of 3D-SMARTER's nanometer- and millisecond-precision, we applied it to quantify the steps of intracellular trafficking via motor proteins. The motion of motor proteins has been demonstrated to be stepwise rather than continuous, with well-defined steps of ∼8 nm.[4,11] Two-dimensional step motions of gold nanoparticles encapsulated

https://doi.org/10.1021/cbmi.5c00293
Chem. Biomed. Imaging XXXX, XXX, XXX−XXX

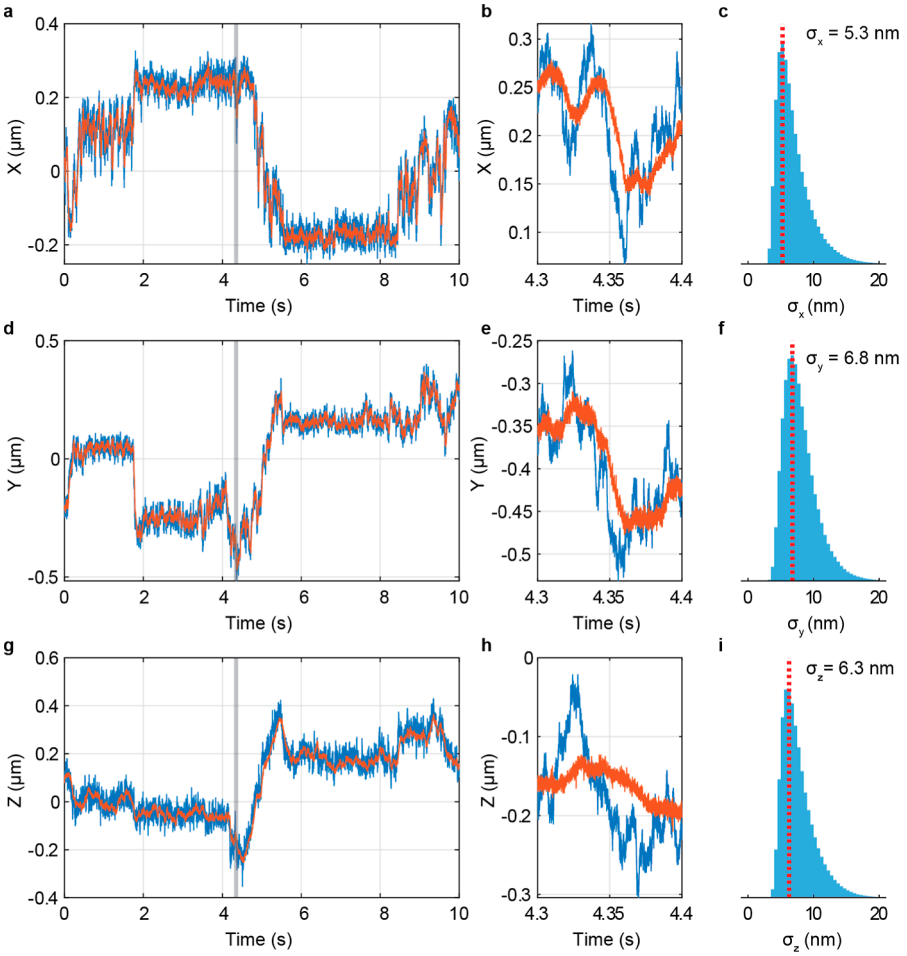

Figure 4. Recursive Bayesian position estimation enables single-microsecond temporal resolution in 3D. (**a,d,g**) Stage positions (orange curve, sampled at 1 kHz) versus Bayesian estimates (blue curve, sampled at 1 MHz) of part of a freely diffusing AgNP trajectory. (**b,e,h**) Closer look at part of the amplitudes in (a,d,g). (**c,f,i**) Distribution of uncertainty from Bayesian estimates.

in vesicles in cells were reported in a previous study using dark-field single-particle tracking microscopy.[4] These small steps require nanometer localization precision and fast and consistent sampling. Here, unfunctionalized 100 nm AgNPs were incubated with live HeLa cells (see Supporting Information). After incubation, AgNPs were internalized into cells via endocytosis[58,59] and tracked with 3D-SMARTER. The depolarized AgNP signal in live cells exhibits a sufficient signal-to-background ratio for 3D-SMARTER tracking (Figures S5, S6). The background from cells is higher than from reflection from the interface, so it is important to consider the reduction in the signal-to-background ratio due to the presence of scattering live cells, particularly in the case of nonuniform background. In the case of nonuniform background, small deviations in the accuracy of the localization may occur. As an example, since the signal-to-background ratio is about 3:1 in live cells, this suggests 25% of the arriving photons actually report the mean position of the background. The degree to which this affects the accuracy of the particle localization will depend on the degree of nonuniformity in the background. It was observed that AgNPs frequently exhibit linear trafficking behavior. Instead of only using the two-dimensional particle positions, the 3D trajectory data points were projected along a central axis and the linear steps were analyzed (Figure 3d,e). An average step size of 7.6 ± 2.5 nm was measured (Figure 3f; see Supplementary Methods for details on step detection), comparable to prior studies.[4,60−63] We note here that it is critical to measure these transport processes in three dimensions to achieve accurate results, as two-dimensional projections can underestimate both displacements and velocities, as has been shown for viral trafficking within cells.[64]

MHz Localization in Three Dimensions with Recursive Bayesian Position Estimates

In RT-3D-SPT, active feedback is used to center the object within the observation volume in real time. If the feedback speed is faster than the process in question, then the current position of the piezoelectric stage should be an excellent approximation for the true particle position. For example, in the results discussed above, stage positions sampled at 1 kHz were treated as the true particle positions. High-end piezo nanopositioners are bandwidth-limited to 1 kHz, which serves as a low-pass filter on the tracked particle position. This is not usually a barrier in fluorescent-based RT-3D-SPT experiments, due to the fact that the fluorescence emission rate limits the sampling rate, rather than the mechanical response time of the stage. However, given the extremely high photon flux from the AgNP in these experiments, sampling far beyond this 1 kHz barrier is possible. Given the >3 MHz scattering rate, we were able to process photon arrivals into 1 μs bins and use a recursive Bayesian analysis to untangle the true particle position from the relatively slow response of the piezoelectric

https://doi.org/10.1021/cbmi.5c00293
Chem. Biomed. Imaging XXXX, XXX, XXX−XXX

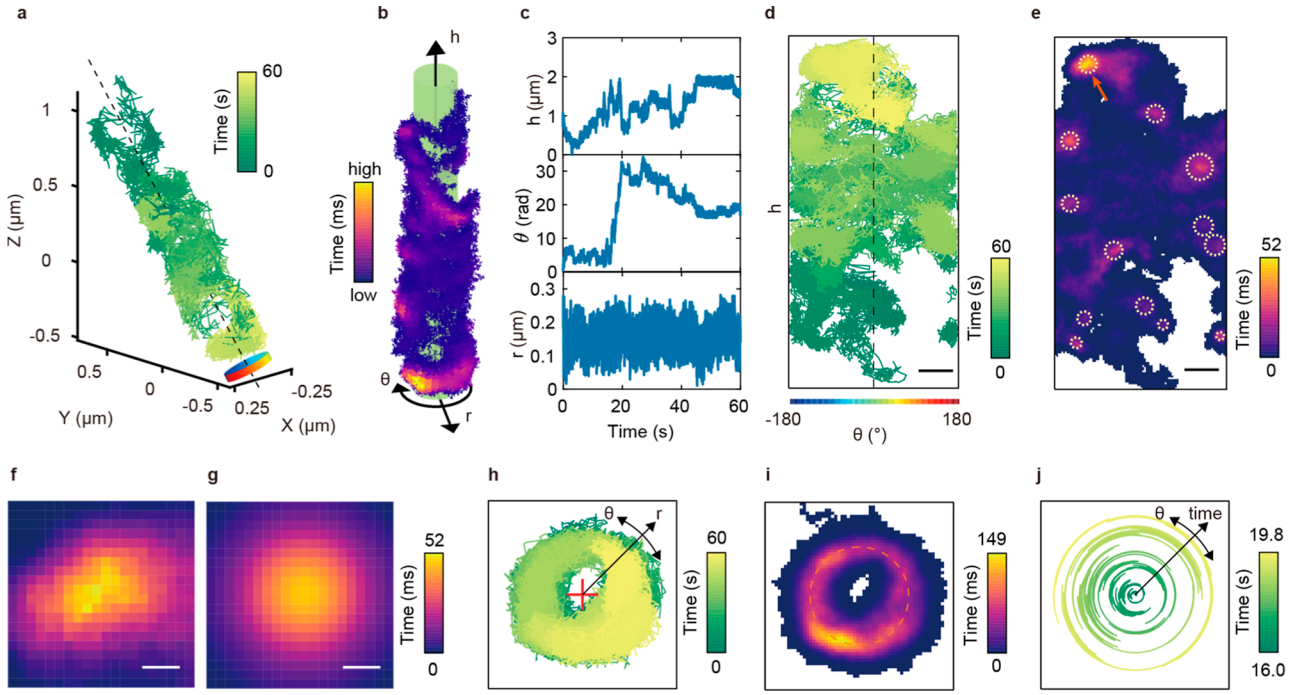

Figure 5. Mapping the nanoscale structure of filopodium with microsecond resolution by 3D-SMARTER. (**a**) 60 s trajectory (sampled at 500 Hz) showing restricted diffusion on a cylindrical structure. (**b**) Demonstration of cylindrical coordinate system overlapped with the trajectory in (a) coded with dwell time in 30 × 30 nm areas. (**c**) r, θ and h versus time from the trajectory in (a). Data sampled at 1 kHz. θ was expanded beyond ±180° for smooth visualization. (d) 2D trajectory of the trajectory in (a) projected onto the cylinder shown in (b) with a radius of 157 nm (average of r shown in (c)). The dashed line is consistent with the dashed line in (b), and the color bar at the bottom showing the angle was consistent with the curved color bars in (a) and (b). Data sampled at 1 kHz. (e) Density map of residence time of 2D trajectory sampled at 1 MHz. Dashed circles show AOIs. (f) Residence time distribution of AOI labeled with orange arrow in (e). (g) 2D Gaussian fit with a σ of 50 nm of data shown in (f). Scale bars in (f) and (g): 50 nm. (h) Trajectory observed from the top of the h-axis in (b). Red cross mark indicates the center of the cylinder and is of 100 × 100 nm size. Data sampled at 1 kHz. (i) Density map of residence time of 2D trajectory shown in (h) sampled at 1 MHz. Dashed circle shows the average of all measured r positions and is of 157 nm radius. (j) Angle versus time of part of the trajectory in (a). The growing radius of the helix plot indicates time progress.

stage (Figure S7). The result is 3D particle tracking at 1 MHz sampling rate. The 1 μs binned photons are used to localize the particle in three dimensions, treating XY and Z as linearly independent. Details of the calculation are provided in Supplementary Note 1. The reconstructed trajectory shows that the stage position effectively acts as a low-pass filter of the best estimate of the particle position (Figure 4a,d,g). The stage position lags behind particle motions estimated by the recursive Bayesian estimate, especially during fast motions (Figure 4b,e,f). Notably, the localization uncertainty of the estimated X/Y positions is comparable to that of the Z position, despite a larger PSF scale in Z and a doubled stage readout error, indicating that similar information efficiency can be achieved across the three dimensions. Further analysis showed that MHz Bayesian reconstructed positions exhibited larger fluctuations than stage positions, and that the standard deviation of estimated positions and stage fluctuations was larger when the particle was actively diffusing than when held static in a cellular context (Figure S15).

AgNP Tracking Reveals Interactions Between AgNPs and Local Hot Spots on HeLa Cell Filopodium

Filopodia are thin cell membrane protrusions that play a significant role in cell adhesion, migration, and endocytosis.[65,66] Filopodia also play an important role in viral infection, where viral "surfing" is frequently observed.[67−69] Despite their extensive involvement in a variety of biological processes, the details of interactions between filopodia and cargos in live cells remain unclear due to the lack of methodologies that can visualize such interactions with sufficient 3D spatiotemporal resolution. With 3D-SMARTER microscopy and AgNPs as bright, durable probes, it is possible to track cargo-filopodium interactions over extended observation times with high 3D spatiotemporal precision. Here, we investigate confined particle diffusion on a cylindrical structure on the live cell surface, including identification of diffusive "hot spots" and characterization of rotational movements. We found that cargo-filopodium interactions display additional spatial complexity compared to the previously discussed longitudinal diffusion driven by motor proteins. Here we utilized 3D-SMARTER to observe the interactions between HIV cell-penetrating TAT peptide (TATp)[70,71] functionalized AgNP (TATp-AgNP) and HeLa cell filopodia. To functionalize the AgNP with TATp, streptavidin (SA) was first labeled with a thiol group (SH) via NHS-PEG-SH to give the protein an affinity for the AgNP surface. After mixing AgNPs with SA-SH, the resulting particles were incubated with TATp-biotin to functionalize the AgNPs with TATp. It was observed that upon functionalization with TATp, AgNP had a larger size (~140 nm diameter functionalized compared to ~100 nm diameter nonfunctionalized) while the absorption spectrum remained unchanged (Figure S8a,b). It was also observed that the emission rate of AgNPs remains unchanged after functionalization and is internalized by a cell (Figure S8c), indicating the stability and robustness of AgNPs despite reports that AgNPs can undergo degradation when captured by cells.[72] TATp-

https://doi.org/10.1021/cbmi.5c00293
Chem. Biomed. Imaging XXXX, XXX, XXX−XXX

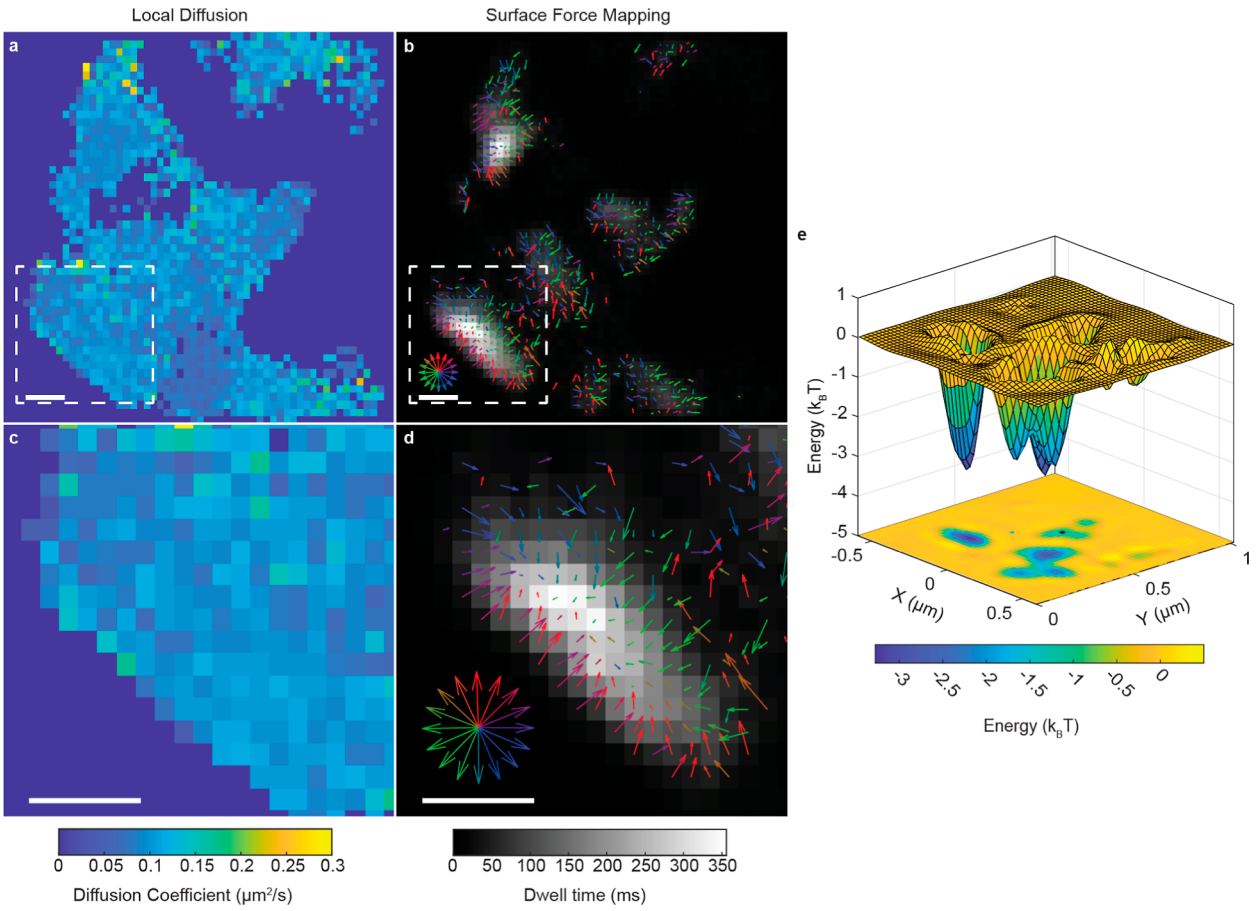

Figure 6. Extracting force-vectors and nanoscale potential wells on 3D surfaces. (**a**) Map of the MLE diffusion coefficient on the surface of a filopodium, carved out by the motion of a single AgNP, localized at 1 μs intervals. (**b**) Zoom in on the square area shown in the top panel. (**c**) MLE extracted force-vectors (arrows) overlaid with the dwell time at each grid position (grayscale). (**d**) Zoom in of square area shown in top panel. (**e**) Potential surface on the surface of a nanoscale filopodium. Scale bars: 100 nm. Scale arrows: 0.1 pN.

AgNPs were added to live HeLa cells and then tracked by 3D-SMARTER. The positive charge of the TATp peptide gave the AgNPs an affinity for the cell membrane. It was observed that a higher concentration (56 μM) of TATp resulted in a higher incidence of intracellular trafficking events (19 out of 27) compared to a lower TATp concentration (0.28 μM, 12 out of 55), as is shown in Figure S9. This observation was consistent with previous studies indicating that nanoparticles with higher TATp valency were more likely to undergo endocytosis.[73−75] AgNPs labeled with arginine-9 (R9) peptides at high concentration comparable to TATp showed a similar high percentage of internalization (18 out of 22). This further indicates that the surface charge dominated the fate of functionalized AgNP.

Among bound particles, cylindrical diffusion on the surface of live HeLa cells was often observed. An example of such motion is shown in Figure 5, for a single trajectory lasting over 15 min and with an average intensity of 2.4 MHz. The complete trajectory shown in Figure 5 overlapped with the cell is shown in Figure S10. The 3D trajectory carves out a cylindrical structure with a diameter of 346 ± 86 nm (Figure S11a). Taking the hydrated diameter of TATp-functionalized AgNP particle (~140 nm) into account, the actual diameter of the tubular structure is ~200 nm, consistent with the reported size of filopodial structures.[65,76] Part of the trajectory with 60 s duration length (900 s−960 s in the entire data set mentioned above) is shown in Figure 5a. There was significant heterogeneity in dwell time at different areas, and the cylindrical geometry is even more pronounced when the trajectory is projected onto a cylindrical coordinate system (r, radius; θ angle; h, height; Figure 5b,c). The same trajectory segment observed from the top of the cylinder in Figure 5b is shown in Figure 5h, and the 2D density of Figure 5h is shown in Figure 5i, which further illustrates the particle undergoing restricted diffusion on a cylindrical surface. A residence-time analysis was performed to determine whether the particle interacted with specific structures on the surface of the filopodium. The coordinates of the trajectory were first projected to the surface of a cylinder with a radius of the average r of the segment (Figure 5d). Analysis performed by projecting onto a cylinder with the AgNP size subtracted yielded similar results (Figure S14). The coordinates from 1 MHz Bayesian reconstruction were then converted to a 2D density map with 10 × 10 nm grids, as shown in Figure 5e. The density map shows the particle covered most of the surface of the cylinder during diffusion while the residence time at different regions varies significantly with local "hot spots" (or areas of interest (AOIs)) which are clearly observable as indicated with circles in Figure 5e. Pixelated intensity in each AOI was approximated as a 2D Gaussian distribution defined as

$$I = Ae^{-(x-x_0^2)+(y-y_0^2)/2\sigma^2}$$

https://doi.org/10.1021/cbmi.5c00293
Chem. Biomed. Imaging XXXX, XXX, XXX−XXX

Here, I is the dwell time of the particle at a given pixel, A is a prefactor, x_0 and y_0 are the center coordinates of the Gaussian spot, and σ is the uncertainty of the spot. Figure 5f−g shows the brightest AOI in Figure 5e and its 2D Gaussian fitting image. The border of a given AOI is defined as a circle within 1.96 σ (95% confidence interval) of the center of the AOI in the 2D density map. Most of the AOIs are repeatedly visited, in some cases two visits are >30 s apart, indicating that the dwelling events could originate from potential structures interacting with the AgNP. The residence time distribution is well fit by a 2-factor exponential decay with half-lives of 0.28 and 5.96 s (Figure S12). Interestingly, the density map from simulated random walks does not display hot spots with comparable residence times to those observed in the experimental data, and residence times in the simulated data show 1-parameter exponential decay (Figure S16). These results indicate residence events with longer half-life cannot be accounted for by random diffusion on the filopodium surface. MSD analysis shows strong confinement within these long dwell areas (Figure S20). Additional measurements on bare AgNPs and AgNPs functionalized with a high density of TATp showed that a higher degree of surface functionalization resulted in longer residence in hot spots (Figure S17), indicating that restriction in hot spots potentially originates from electrostatic interactions.

We also investigated the speed and direction of rotational (motion in θ direction) diffusion on the filopodium. Figure 5j shows the angular position as a function of time, in which the particle underwent a rapid clockwise rotation over 3.8 s. After labeling and analyzing fast-rotation events across 13 intervals, no significant difference in rotation speed or directionality was observed, with 52 clockwise events at 13.5 ± 6.4 rads/s and 60 counterclockwise events at 15.3 ± 7.5 rads/s (Figure S11b−d). This indicates that the cylindrical motion was random, rather than biased in a particular direction. It should be noted that these high spatiotemporal resolution dynamic features of TATp-AgNPs are only obtainable with the MHz recursive Bayesian reconstruction method and cannot be acquired using only the piezo stage as a readout of the particle's position (Figure S13).

Surface Force Mapping Shows Local Potential Wells Overlapped with High Residence Time AOIs

With sufficient spatial and temporal resolution, it is possible to extract more information than just the local diffusion coefficient from trajectories. A moving particle on a complex surface will experience areas of different viscosity, physical barriers, and local potentials. Measuring these local potentials requires localization and temporal precision on the scale of the potentials involved. The spatiotemporal precision enabled by 3D-SMARTER here allows mapping of forces on complex 3D surfaces with nanoscale resolution. The process applied here is derived from a Bayesian algorithm developed by Masson and co-workers.[77] Briefly, to measure both the isotropic diffusion and local drift velocity simultaneously, the data are gridded, and the following likelihood is applied to each gridded position:

$$P(\Delta r|F_{i,j}, D_{i,j}, \tau) = \frac{1}{4\pi(D_{i,j}\tau + \sigma^2)} e^{-(\Delta r - F_{i,j}\tau/\gamma_{i,j})^2/4(D_{i,j}\tau+\sigma^2)}$$

The equation gives the probability of observing a displacement (Δr) given a particular grid position (i,j), delay time (τ), local diffusion coefficient ($D_{i,j}$), local force ($F_{i,j}$), local drag coefficient ($\gamma_{i,j}$), and measurement noise (σ). By multiplying the probability for each observed displacement, a maximum likelihood estimate (MLE) can be extracted for both the local diffusion coefficient $D_{i,j}$ and local vector forces $F_{i,j}$, which can be used to extract the scalar potential. A full description of the calculation of force vectors is provided in Supplementary Note 2. The results of this analysis on a 60 s segment of filopodial surface diffusion are shown in Figure 6. There is a striking difference between the map of the MLE estimated diffusion coefficients (Figure 6a,c) and the density of spots at each gridded position (Figure 6b,d). There seems to be no correlation between the diffusion coefficient and the amount of time a particle spends in a particular hotspot. In contrast, the MLE-estimated force vectors indicate that particles are constrained to nanoscale domains by directional motion, which pushes them back into small areas. This indicates that these hot spots are not simply pockets of altered viscosity but are actual potential wells that trap the particle in a particular domain. Surface integration of the force vectors enables full reconstruction of the nanoscale potentials on the filopodium surface, as shown in Figure 6e.

CONCLUSION

In this study, we introduce 3D-SMARTER, a real-time tracking method that utilizes depolarized detection of AgNPs. The combination of AgNPs and rapid feedback tracking of 3D-SMART provides a large sampling depth of over 50 μm, spatial precision down to 2−4 nm in XYZ, and temporal sampling down to 1 μs. Critically, the microsecond temporal resolution and nanometer localization precision can be extracted from a single trajectory with duration exceeding tens of minutes in a live cell. While many processes in live cells happen on slower time scales, the combined nanometer and microsecond spatiotemporal resolution presented here demonstrates 3D-SMARTER is uniquely suited for microrheology.[78] Nanometer-scale motions over microseconds can provide a wealth of information about the interactions of nanoscale objects with their environment. Moreover, 3D-SMARTER is able to do this on complex 3D surfaces, as shown in this work, uncovering diffusive traps on filopodia. These studies show the power of the high spatial and temporal precision of 3D-SMARTER. When temporal sampling is poor, only changes in the diffusion coefficient can be extracted, and even then, these changes are limited by the spatial resolution of each spot. Here, 3D-SMARTER goes far beyond simple changes in diffusion coefficient, or deviations in the linearity of a mean-square displacement analysis. Drift velocities, their associated force vectors, and even potentials can be extracted with nanoscale precision. Residence time analysis in hot spots and force analysis offer results that can be mutually verified by each other, and the two methods combined are a novel approach to probe 3D confined diffusions and characterize nanoscale domains that are yet to be verified by existing methods. 3D-SMARTER has the potential to provide energy surfaces for a wide range of biological structures, yielding an ever clearer picture of forces at the nanoscale in biology. Due to the high signal intensity and remarkable photostability of scattering signals from plasmonic nanoparticles, these signals exhibit an outstanding signal-to-noise ratio. The technique is readily expandable to other scattering materials, such as gold nanoparticles, by changing the laser wavelength to match the plasmon peak of the material in question. However, background scattering from cells or coverslips can impact the

https://doi.org/10.1021/cbmi.5c00293
Chem. Biomed. Imaging XXXX, XXX, XXX−XXX

performance of 3D-SMARTER. If the plasmonic nanoparticles are too small, their relatively weaker scattering signals could be masked by the fluctuating scattering signals from cells, impeding efficient 3D tracking. To address this issue, future studies could utilize dark-field illumination to attain an even higher signal-to-background ratio, facilitating 3D-SMARTER for smaller particle tracking and yielding improved spatial precision. Anisotropic scattering probes, such as nanorods, can also be explored in 3D-SMARTER to study the rotational potentials on complex biological surfaces,[49,79−81] adding yet another dimension to this powerful method.

■ ASSOCIATED CONTENT

Data Availability Statement

Raw data files for 3D-SMARTER trajectories can be found at the Duke University Research Data Repository at https://doi.org/10.7924/R4DV1Q87F. Code availability Code to analyze 3D-SMARTER trajectories with MATLAB is available at https://github.com/welsherlab/3DSMARTER.

Supporting Information

The Supporting Information is available free of charge at https://pubs.acs.org/doi/10.1021/cbmi.5c00293.

Supplementary Methods; Supplementary Notes detailing recursive Bayesian localization and surface force and potential mapping; Supplementary Figures 1−20 (PDF)

■ AUTHOR INFORMATION

Corresponding Authors

Shangguo Hou − *Department of Chemistry, Duke University, Durham, North Carolina 27705, United States; Institute of Systems and Physical Biology, Shenzhen Bay Laboratory, Shenzhen 518132, China;* orcid.org/0000-0001-6394-6467; Email: Shangguo.hou@szbl.ac.cn

Kevin D. Welsher − *Department of Chemistry, Duke University, Durham, North Carolina 27705, United States;* orcid.org/0000-0002-3180-279X; Email: kevin.welsher@duke.edu

Authors

Chen Zhang − *Department of Chemistry, Duke University, Durham, North Carolina 27705, United States; Institute of Systems and Physical Biology, Shenzhen Bay Laboratory, Shenzhen 518132, China;* orcid.org/0000-0003-0193-3948

Anastasia Niver − *Department of Chemistry, Duke University, Durham, North Carolina 27705, United States*

Complete contact information is available at: https://pubs.acs.org/10.1021/cbmi.5c00293

Author Contributions

[§]S.H. and C.Z. contributed equally to this work.

Notes

The authors declare no competing financial interest.

■ ACKNOWLEDGMENTS

The authors acknowledge financial support from the National Institute of General Medical Sciences of the National Institutes of Health under award number R35GM124868, the National Science Foundation under Grant No. 1847899, and from Duke University.

■ REFERENCES

(1) Jin, S.; Haggie, P. M.; Verkman, A. S. Single-particle tracking of membrane protein diffusion in a potential: simulation, detection, and application to confined diffusion of CFTR Cl- channels. *Biophys. J.* **2007**, *93* (3), 1079−1088.

(2) Wang, Z. G.; Wang, L.; Lamb, D. C.; Chen, H. J.; Hu, Y. S.; Wang, H. P.; Pang, D. W.; Liu, S. L. Real-Time Dissecting the Dynamics of Drug Transportation in the Live Brain. *Nano Lett.* **2021**, *21* (1), 642−650.

(3) Mashanov, G. I.; Nenasheva, T. A.; Mashanova, A.; Lape, R.; Birdsall, N. J. M.; Sivilotti, L.; Molloy, J. E. Heterogeneity of cell membrane structure studied by single molecule tracking. *Faraday Discuss.* **2021**, *232* (0), 358−374.

(4) Nan, X.; Sims, P. A.; Xie, X. S. Organelle tracking in a living cell with microsecond time resolution and nanometer spatial precision. *ChemPhysChem* **2008**, *9* (5), 707−712.

(5) Xiang, L. M.; Chen, K.; Yan, R.; Li, W.; Xu, K. Single-molecule displacement mapping unveils nanoscale heterogeneities in intracellular diffusivity. *Nat. Methods* **2020**, *17* (5), 524.

(6) Etoc, F.; Balloul, E.; Vicario, C.; Normanno, D.; Lisse, D.; Sittner, A.; Piehler, J.; Dahan, M.; Coppey, M. Non-specific interactions govern cytosolic diffusion of nanosized objects in mammalian cells (vol 17, pg 740, 2018). *Nat. Mater.* **2018**, *17* (11), 1048.

(7) Masson, J. B.; Dionne, P.; Salvatico, C.; Renner, M.; Specht, C. G.; Triller, A.; Dahan, M. Mapping the Energy and Diffusion Landscapes of Membrane Proteins at the Cell Surface Using High-Density Single-Molecule Imaging and Bayesian Inference: Application to the Multiscale Dynamics of Glycine Receptors in the Neuronal Membrane. *Biophys. J.* **2014**, *106* (1), 74−83.

(8) Wehnekamp, F.; Plucińska, G.; Thong, R.; Misgeld, T.; Lamb, D. C. Nanoresolution real-time 3D orbital tracking for studying mitochondrial trafficking in vertebrate axons in vivo. *Elife* **2019**, *8*, No. e46059.

(9) Ewers, H.; Smith, A. E.; Sbalzarini, I. F.; Lilie, H.; Koumoutsakos, P.; Helenius, A. Single-particle tracking of murine polyoma virus-like particles on live cells and artificial membranes. *Proc. Natl. Acad. Sci. U. S. A.* **2005**, *102* (42), 15110−15115.

(10) Di Rienzo, C.; Gratton, E.; Beltram, F.; Cardarelli, F. Fast spatiotemporal correlation spectroscopy to determine protein lateral diffusion laws in live cell membranes. *Proc. Natl. Acad. Sci. U. S. A.* **2013**, *110* (30), 12307−12312.

(11) Coy, D. L.; Wagenbach, M.; Howard, J. Kinesin takes one 8-nm step for each ATP that it hydrolyzes. *J. Biol. Chem.* **1999**, *274* (6), 3667−3671.

(12) Ando, J.; Shima, T.; Kanazawa, R.; Shimo-Kon, R.; Nakamura, A.; Yamamoto, M.; Kon, T.; Iino, R. Small stepping motion of processive dynein revealed by load-free high-speed single-particle tracking. *Sci. Rep.* **2020**, *10* (1), 1080.

(13) Guo, Y.; Li, D.; Zhang, S.; Yang, Y.; Liu, J.-J.; Wang, X.; Liu, C.; Milkie, D. E.; Moore, R. P.; Tulu, U. S.; et al. Visualizing intracellular organelle and cytoskeletal interactions at nanoscale resolution on millisecond timescales. *Cell* **2018**, *175* (5), 1430−1442.e17.

(14) Thompson, R. E.; Larson, D. R.; Webb, W. W. Precise Nanometer Localization Analysis for Individual Fluorescent Probes. *Biophys. J.* **2002**, *82* (5), 2775−2783.

(15) Digman, M. A.; Caiolfa, V. R.; Zamai, M.; Gratton, E. The phasor approach to fluorescence lifetime imaging analysis. *Biophys. J.* **2008**, *94* (2), L14−L16.

(16) Levi, V.; Ruan, Q.; Kis-Petikova, K.; Gratton, E. Scanning FCS, a novel method for three-dimensional particle tracking. *Biochem. Soc. Trans.* **2003**, *31*, 997−1000.

(17) Cang, H.; Wong, C. M.; Xu, C. S.; Rizvi, A. H.; Yang, H. Confocal three dimensional tracking of a single nanoparticle with concurrent spectroscopic readouts. *Appl. Phys. Lett.* **2006**, *88* (22), 223901.

(18) Lessard, G. A.; Goodwin, P. M.; Werner, J. H. Three-dimensional tracking of fluorescent particles. *Ultrasensitive and Single-*

Molecule Detection Technologies, Proceedings SPIE BIOS, San Jose, California, 2006, *6092*..
(19) McHale, K.; Berglund, A. J.; Mabuchi, H. Quantum dot photon statistics measured by three-dimensional particle tracking. *Nano Lett.* **2007**, *7* (11), 3535−3539.
(20) Katayama, Y.; Burkacky, O.; Meyer, M.; Brauchle, C.; Gratton, E.; Lamb, D. C. Real-Time Nanomicroscopy via Three-Dimensional Single-Particle Tracking. *ChemPhysChem* **2009**, *10* (14), 2458−2464.
(21) Germann, J. A.; Davis, L. M. Three-dimensional tracking of a single fluorescent nanoparticle using four-focus excitation in a confocal microscope. *Opt. Express* **2014**, *22* (5), 5641−5650.
(22) Perillo, E. P.; Liu, Y. L.; Huynh, K.; Liu, C.; Chou, C. K.; Hung, M. C.; Yeh, H. C.; Dunn, A. K. Deep and high-resolution three-dimensional tracking of single particles using nonlinear and multiplexed illumination. *Nat. Commun.* **2015**, *6*, 7874.
(23) Ashley, T. T.; Gan, E. L.; Pan, J.; Andersson, S. B. Tracking single fluorescent particles in three dimensions via extremum seeking. *Biomed. Opt. Express* **2016**, *7* (9), 3355−3376.
(24) Hou, S.; Lang, X.; Welsher, K. Robust real-time 3D single-particle tracking using a dynamically moving laser spot. *Opt. Lett.* **2017**, *42* (12), 2390−2393.
(25) Tan, X.; Hou, S.; Niver, A.; Zhang, C.; Johnson, A.; Welsher, K. D. Active-Feedback 3D Single-Molecule Tracking Using a Fast-Responding Galvo Scanning Mirror. *J. Phys. Chem. A* **2023**, *127* (30), 6320−6328.
(26) Levi, V.; Ruan, Q. Q.; Gratton, E. 3-D particle tracking in a two-photon microscope: Application to the study of molecular dynamics in cells. *Biophys. J.* **2005**, *88* (4), 2919−2928.
(27) Hou, S.; Johnson, C.; Welsher, K. Real-Time 3D Single Particle Tracking: Towards Active Feedback Single Molecule Spectroscopy in Live Cells. *Molecules* **2019**, *24* (15), 2826.
(28) Jiang, C.; Yang, M.; Li, W.; Dou, S.-X.; Wang, P.-Y.; Li, H. Spatiotemporal three-dimensional transport dynamics of endocytic cargos and their physical regulations in cells. *Iscience* **2022**, *25* (5), 104210.
(29) Liu, Y.-L.; Perillo, E. P.; Ang, P.; Kim, M.; Nguyen, D. T.; Blocher, K.; Chen, Y.-A.; Liu, C.; Hassan, A. M.; Vu, H. T.; et al. Three-dimensional two-color dual-particle tracking microscope for monitoring DNA conformational changes and nanoparticle landings on live cells. *ACS Nano* **2020**, *14* (7), 7927−7939.
(30) Knight, S. C.; Xie, L.; Deng, W.; Guglielmi, B.; Witkowsky, L. B.; Bosanac, L.; Zhang, E. T.; El Beheiry, M.; Masson, J.-B.; Dahan, M.; et al. Dynamics of CRISPR-Cas9 genome interrogation in living cells. *Science* **2015**, *350* (6262), 823−826.
(31) Xiao, L. H.; Yeung, E. S. Optical Imaging of Individual Plasmonic Nanoparticles in Biological Samples. *Annu. Rev. Anal. Chem.* **2014**, *7*, 89−111.
(32) Arroyo, J. O.; Kukura, P. Non-fluorescent schemes for single-molecule detection, imaging and spectroscopy. *Nat. Photonics* **2016**, *10* (1), 11−17.
(33) Chen, T.; Dong, B.; Chen, K.; Zhao, F.; Cheng, X.; Ma, C.; Lee, S.; Zhang, P.; Kang, S. H.; Ha, J. W.; et al. Optical Super-Resolution Imaging of Surface Reactions. *Chem. Rev.* **2017**, *117* (11), 7510−7537.
(34) Taylor, A. B.; Zijlstra, P. Single-Molecule Plasmon Sensing: Current Status and Future Prospects. *ACS Sens.* **2017**, *2* (8), 1103−1122.
(35) Willets, K. A.; Wilson, A. J.; Sundaresan, V.; Joshi, P. B. Super-Resolution Imaging and Plasmonics. *Chem. Rev.* **2017**, *117* (11), 7538−7582.
(36) Zhao, M.; Chen, P. Exploring Plasmonic Photocatalysis via Single-Molecule Reaction Imaging. *Nano Lett.* **2020**, *20* (5), 2939−2940.
(37) Han, X. X.; Rodriguez, R. S.; Haynes, C. L.; Ozaki, Y.; Zhao, B. Surface-enhanced Raman spectroscopy. *Nat. Rev. Methods Primers* **2021**, *1* (1), 87.
(38) Chen, K.; Gu, Y.; Sun, W.; Dong, B.; Wang, G.; Fan, X.; Xia, T.; Fang, N. Characteristic rotational behaviors of rod-shaped cargo revealed by automated five-dimensional single particle tracking. *Nat. Commun.* **2017**, *8* (1), 887.
(39) Poon, C.-Y.; Wei, L.; Xu, Y.; Chen, B.; Xiao, L.; Li, H.-W. Quantification of cancer biomarkers in serum using scattering-based quantitative single particle intensity measurement with a dark-field microscope. *Anal. Chem.* **2016**, *88* (17), 8849−8856.
(40) Wei, L.; Ma, Y.; Zhu, X.; Xu, J.; Wang, Y.; Duan, H.; Xiao, L. Sub-diffraction-limit localization imaging of a plasmonic nanoparticle pair with wavelength-resolved dark-field microscopy. *Nanoscale* **2017**, *9* (25), 8747−8755.
(41) Ueno, H.; Nishikawa, S.; Iino, R.; Tabata, K. V.; Sakakihara, S.; Yanagida, T.; Noji, H. Simple dark-field microscopy with nanometer spatial precision and microsecond temporal resolution. *Biophys. J.* **2010**, *98* (9), 2014−2023.
(42) Herrmann, L. O.; Baumberg, J. J. Watching single nanoparticles grow in real time through supercontinuum spectroscopy. *Small* **2013**, *9* (22), 3743−3747.
(43) Spindler, S.; Ehrig, J.; König, K.; Nowak, T.; Piliarik, M.; Stein, H. E.; Taylor, R. W.; Garanger, E.; Lecommandoux, S.; Alves, I. D.; et al. Visualization of lipids and proteins at high spatial and temporal resolution via interferometric scattering (iSCAT) microscopy. *J. Phys. D: Appl. Phys.* **2016**, *49* (27), 274002.
(44) Yang, M.; Batey, J. E.; Dong, B. Automated Five-Dimensional Single Particle Tracking by Bifocal Parallax Dark-Field Microscopy with Electronic Tunable Lens. *Anal. Chem.* **2024**, *96* (1), 1−5.
(45) Cheng, X.; Chen, K.; Dong, B.; Yang, M.; Filbrun, S. L.; Myoung, Y.; Huang, T. X.; Gu, Y.; Wang, G.; Fang, N. Dynamin-dependent vesicle twist at the final stage of clathrin-mediated endocytosis. *Nat. Cell Biol.* **2021**, *23* (8), 859−869.
(46) Taylor, R. W.; Mahmoodabadi, R. G.; Rauschenberger, V.; Giessl, A.; Schambony, A.; Sandoghdar, V. Interferometric scattering microscopy reveals microsecond nanoscopic protein motion on a live cell membrane. *Nat. Photonics* **2019**, *13* (7), 480−487.
(47) Cang, H.; Montiel, D.; Xu, C. S.; Yang, H. Observation of spectral anisotropy of gold nanoparticles. *J. Chem. Phys.* **2008**, *129* (4), 044503.
(48) Xu, C. S.; Cang, H.; Montiel, D.; Yang, H. Rapid and quantitative sizing of nanoparticles using three-dimensional single-particle tracking. *J. Phys. Chem. C* **2007**, *111* (1), 32−35.
(49) Beckwith, J. S.; Yang, H. Sub-millisecond Translational and Orientational Dynamics of a Freely Moving Single Nanoprobe. *J. Phys. Chem. B* **2021**, *125* (49), 13436−13443.
(50) Hou, S.; Exell, J.; Welsher, K. Real-time 3D single molecule tracking. *Nat. Commun.* **2020**, *11* (1), 3607.
(51) Zhang, C.; Welsher, K. Information-Efficient, Off-Center Sampling Results in Improved Precision in 3D Single-Particle Tracking Microscopy. *Entropy (Basel)* **2021**, *23* (5), 498.
(52) Bujak, Ł.; Holanová, K.; Garcia Marin, A.; Henrichs, V.; Barvík, I.; Braun, M.; Lánský, Z.; Piliarik, M. Fast leaps between millisecond confinements govern Ase1 diffusion along microtubules. *Small Methods* **2021**, *5* (10), 2100370.
(53) Lerner, J.; Gomez-Garcia, P. A.; McCarthy, R. L.; Liu, Z.; Lakadamyali, M.; Zaret, K. S. Two-parameter mobility assessments discriminate diverse regulatory factor behaviors in chromatin. *Mol. Cell* **2020**, *79* (4), 677−688.
(54) Hou, S.; Welsher, K. An Adaptive Real-Time 3D Single Particle Tracking Method for Monitoring Viral First Contacts. *Small* **2019**, *15* (44), No. e1903039.
(55) Johnson, C.; Exell, J.; Lin, Y.; Aguilar, J.; Welsher, K. D. Capturing the start point of the virus−cell interaction with high-speed 3D single-virus tracking. *Nat. Methods* **2022**, *19*, 1642.
(56) Fields, A. P.; Cohen, A. E. Optimal tracking of a Brownian particle. *Opt. Express* **2012**, *20* (20), 22585−22601.
(57) Wäldchen, S.; Lehmann, J.; Klein, T.; van de Linde, S.; Sauer, M. Light-induced cell damage in live-cell super-resolution microscopy. *Sci. Rep.* **2015**, *5* (1), 15348.
(58) Wu, M. Y.; Guo, H. B.; Liu, L.; Liu, Y.; Xie, L. M. Size-dependent cellular uptake and localization profiles of silver nanoparticles. *Int. J. Nanomed.* **2019**, *14*, 4247−4259.

https://doi.org/10.1021/cbmi.5c00293
Chem. Biomed. Imaging XXXX, XXX, XXX−XXX

(59) AshaRani, P. V.; Hande, M. P.; Valiyaveettil, S. Anti-proliferative activity of silver nanoparticles. *BMC Cell Biol.* **2009**, *10*, 65.
(60) Svoboda, K.; Schmidt, C. F.; Schnapp, B. J.; Block, S. M. Direct Observation of Kinesin Stepping by Optical Trapping Interferometry. *Nature* **1993**, *365* (6448), 721−727.
(61) Coppin, C. M.; Finer, J. T.; Spudich, J. A.; Vale, R. D. Detection of sub-8-nm movements of kinesin by high-resolution optical-trap microscopy. *Proc. Natl. Acad. Sci. U. S. A.* **1996**, *93* (5), 1913−1917.
(62) Mallik, R.; Carter, B. C.; Lex, S. A.; King, S. J.; Gross, S. P. Cytoplasmic dynein functions as a gear in response to load. *Nature* **2004**, *427* (6975), 649−652.
(63) Kural, C.; Kim, H.; Syed, S.; Goshima, G.; Gelfand, V. I.; Selvin, P. R. Kinesin and Dynein Move a Peroxisome in Vivo: A Tug-of-War or Coordinated Movement? *Science* **2005**, *308* (5727), 1469−1472.
(64) Lin, Y.; Exell, J.; Lin, H.; Zhang, C.; Welsher, K. D. Hour-Long Kilohertz Sampling Rate Three-Dimensional Single-Virus Tracking in Live Cells Enabled by StayGold Fluorescent Protein Fusions. *J. Phys. Chem. B* **2024**, *128* (23), 5590−5600.
(65) Mattila, P. K.; Lappalainen, P. F. molecular architecture and cellular functions. *Nat. Rev. Mol. Cell Biol.* **2008**, *9* (6), 446−454.
(66) Jacquemet, G.; Hamidi, H.; Ivaska, J. Filopodia in cell adhesion, 3D migration and cancer cell invasion. *Curr. Opin. Cell Biol.* **2015**, *36*, 23−31.
(67) Dixit, R.; Tiwari, V.; Shukla, D. Herpes simplex virus type 1 induces filopodia in differentiated P19 neural cells to facilitate viral spread. *Neurosci. Lett.* **2008**, *440* (2), 113−118.
(68) Sherer, N. M.; Lehmann, M. J.; Jimenez-Soto, L. F.; Horensavitz, C.; Pypaert, M.; Mothes, W. Retroviruses can establish filopodial bridges for efficient cell-to-cell transmission. *Nat. Cell Biol.* **2007**, *9* (3), 310−315.
(69) Lehmann, M. J.; Sherer, N. M.; Marks, C. B.; Pypaert, M.; Mothes, W. Actin- and myosin-driven movement of viruses along filopodia precedes their entry into cells. *J. Cell Biol.* **2005**, *170* (2), 317−325.
(70) Schmidt, N.; Mishra, A.; Lai, G. H.; Wong, G. C. L. Arginine-rich cell-penetrating peptides. *FEBS Lett.* **2010**, *584* (9), 1806−1813.
(71) Stewart, K. M.; Horton, K. L.; Kelley, S. O. Cell-penetrating peptides as delivery vehicles for biology and medicine. *Org. Biomol. Chem.* **2008**, *6* (13), 2242−2255.
(72) Porter, G.; Duncan, W.; Jude, A.; Abdelmoneim, D.; Easingwood, R.; Coates, D. Endocytosed silver nanoparticles degrade in lysosomes to form secondary nanoparticle structures during expression of autophagy genes in osteogenic cells. *Nanomedicine: Nanotechnology, Biology and Medicine* **2021**, *33*, 102355.
(73) Suzuki, Y.; Roy, C. N.; Promjunyakul, W.; Hatakeyama, H.; Gonda, K.; Imamura, J.; Vasudevanpillai, B.; Ohuchi, N.; Kanzaki, M.; Higuchi, H.; et al. Single Quantum Dot Tracking Reveals that an Individual Multivalent HIV-1 Tat Protein Transduction Domain Can Activate Machinery for Lateral Transport and Endocytosis. *Mol. Cell. Biol.* **2013**, *33* (15), 3036−3049.
(74) Kawamura, K. S.; Sung, M.; Bolewska-Pedyczak, E.; Gariépy, J. Probing the Impact of Valency on the Routing of Arginine-Rich Peptides into Eukaryotic Cells. *Biochemistry* **2006**, *45* (4), 1116−1127.
(75) Zhao, M.; Kircher, M. F.; Josephson, L.; Weissleder, R. Differential Conjugation of Tat Peptide to Superparamagnetic Nanoparticles and Its Effect on Cellular Uptake. *Bioconjugate Chem.* **2002**, *13* (4), 840−844.
(76) Mitchison, T. J.; Cramer, L. P. Actin-based cell motility and cell locomotion. *Cell* **1996**, *84* (3), 371−379.
(77) Voisinne, G.; Alexandrou, A.; Masson, J.-B. Quantifying Biomolecule Diffusivity Using an Optimal Bayesian Method. *Biophys. J.* **2010**, *98* (4), 596−605.
(78) Crocker, J. C.; Valentine, M. T.; Weeks, E. R.; Gisler, T.; Kaplan, P. D.; Yodh, A. G.; Weitz, D. A. Two-point microrheology of inhomogeneous soft materials. *Phys. Rev. Lett.* **2000**, *85* (4), 888−891.
(79) Chen, K.; Gu, Y.; Sun, W.; Dong, B.; Wang, G.; Fan, X.; Xia, T.; Fang, N. Characteristic rotational behaviors of rod-shaped cargo revealed by automated five-dimensional single particle tracking. *Nat. Commun.* **2017**, *8* (1), 887.
(80) Cheng, X.; Chen, K.; Dong, B.; Yang, M.; Filbrun, S. L.; Myoung, Y.; Huang, T.-X.; Gu, Y.; Wang, G.; Fang, N. Dynamin-dependent vesicle twist at the final stage of clathrin-mediated endocytosis. *Nat. Cell Biol.* **2021**, *23* (8), 859−869.
(81) Mazaheri, M.; Ehrig, J.; Shkarin, A.; Zaburdaev, V.; Sandoghdar, V. Ultrahigh-Speed Imaging of Rotational Diffusion on a Lipid Bilayer. *Nano Lett.* **2020**, *20* (10), 7213−7219.

https://doi.org/10.1021/cbmi.5c00293
Chem. Biomed. Imaging XXXX, XXX, XXX−XXX